processes

MDPI

Article

Turbulent Frictional Drag of Weighted Fracturing Fluids in Pipes: Experiments and Large-Eddy Simulations

Jianxin Peng [1,2,3,4,†], Ying Gao [5,†], Jueyong Feng [1,2,3,4], Xin Qiao [1,2,3,4], Lili Li [1,2,3,4], Liwei Wang [5], Wen Zhang [6], Yanyan Feng [6,*] and Zhenlin Li [6]

[1] CNPC Tarim Petroleum Oil and Gas Technology Research Institute, Korla 841000, China; pengjx-tlm@petrochina.com.cn (J.P.); fjy-tlm@petrochina.com.cn (J.F.); qiaox-tlm@petrochina.com.cn (X.Q.); lilili-tlm@petrochina.com.cn (L.L.)
[2] CNPC R&D Center for Ultra-Deep Complex Reservoir Exploration and Development Technology, Korla 841000, China
[3] Xinjiang Uygur Autonomous Region Engineering Research Center for Ultra-Deep Complex Reservoir Exploration and Development, Korla 841000, China
[4] Xinjiang Key Laboratory of Ultra-Deep Oil and Gas, Korla 841000, China
[5] Research Institute of Petroleum Exploration and Development, Beijing 100083, China; gaoying69@petrochina.com.cn (Y.G.); wangliwei69@petrochina.com.cn (L.W.)
[6] Beijing Key Laboratory of Process Fluid Filtration and Separation, College of New Energy Science and Engineering, China University of Petroleum, Beijing 102249, China; 15771929671@163.com (W.Z.); zhenlinli@263.net (Z.L.)
* Correspondence: fengyanyan@cup.edu.cn
† These authors contributed equally to this work.

Abstract

With the continuous development of deep oil and gas resources, the role of weighted fracturing fluids in reducing wellhead operating pressure has become increasingly important. However, the turbulent frictional drag behaviors of weighted fracturing fluids in pipes have not been explored systematically. In this study, the frictional drag characteristics and flow behaviors of non-weighted and weighted fracturing fluids in pipes are investigated at different flow rates, densities, pipe diameters, and rheological parameters via steady-state rheological tests and pipe flow friction experiments, together with large-eddy simulation and a power-law constitutive model for generalized Newtonian fluids. The main findings are as follows. The drag reduction rates of non-weighted polyacrylamide solutions basically increase with flow rate, and the optimal molecular weight of 600–700 $\times$ 10^4 corresponds to the highest drag reduction rate of 62%, while excessively large molecular weights weaken drag reduction effectiveness due to enhanced chain entanglement. The types of weighting salts have a significant effect on drag reduction performance. The 20% KCl system obtains the highest drag reduction rate of 64.8%, while the high-density $CaBr_2$ system obtains the lowest rate of 42.3% because of the combined effects of fluid density, polymer concentration, and shear rheological properties. Parameter sensitivity analysis indicates that the power-law index n is the most sensitive parameter controlling frictional drag, followed by pipe diameter D. The novelty of this study lies in integrating experimental investigation, LES, and parameter sensitivity analysis to provide a theoretical basis for deep fracturing working conditions and fracturing fluids design.

Keywords: weighted fracturing fluid; turbulent frictional drag; pipeline friction resistance test; large-eddy simulation; generalized Newtonian fluid; sensitivity analysis

Check for updates

Academic Editor: Tianshou Ma

Received: 28 July 2026
Revised: 23 August 2026
Accepted: 28 August 2026
Published: 2 September 2026

Copyright: © 2026 by the authors. Licensee MDPI, Basel, Switzerland. This article is an open access article distributed under the terms and conditions of the Creative Commons Attribution (CC BY) license.

1. Introduction

As conventional oil and gas resources gradually become depleted, oil and gas exploration and development shift from middle and shallow formations to deep and ultra-deep ones. Hydraulic fracturing has become one of the core engineering technologies for improving the effective development of low-permeability and low-porosity reservoirs [1]. During hydraulic fracturing, frictional drag along the pipe increases rapidly with increasing well depth or flow rate, which may result in excessively high wellhead pressure [2,3]. In engineering practice, weighted fracturing fluids are often employed to reduce wellhead pressure. Adding inorganic- or organic-salt weighting agents into water-based fracturing fluids increases the hydrostatic pressure in the wellbore, thereby lowering the surface pump pressure [4]. The weighting agents commonly used in existing studies include $CaCl_2$, KCl, NaCl, sodium formate, and other organic-salt systems. Weighting agents not only alter the densities of fracturing fluids, but also influence the hydration, crosslinking reaction, and shear-thinning behaviors of polymers, so that weighted fracturing fluids exhibit different rheological characteristics than conventional fracturing fluids [5,6]. Therefore, understanding the turbulent frictional drag behaviors of weighted fracturing fluids in pipes is of great significance for parameter optimization of deep fracturing systems and predicting wellhead pressures.

Water-based fracturing fluids are classified as non-Newtonian fluids containing polymers, crosslinking networks, or surfactant structures, with an apparent viscosity varying with shear rate. They may exhibit shear-thinning, viscoelastic, and other rheological behaviors [7,8]. Toms [9] was the first to discover that adding a small amount of long-chain polymer to Newtonian fluids can significantly reduce the turbulent frictional drag. This phenomenon is widely known as the Toms effect. Based on abundant pipe flow experimental data, Virk [10] proposed the maximum drag reduction asymptote, revealing that the friction factor of polymer solutions is essentially different from the Blasius empirical relationship for Newtonian fluids. Lumley [11] elucidated drag-reducing mechanisms based on the influence of polymers on small-scale turbulent structures and viscous effects. Choueiri et al. [12] further pointed out that the elastic effect of polymers may cause drag reduction to exceed the conventional asymptotic limit.

In terms of experimental studies, Escudier et al. [13] conducted turbulent flow experiments in circular pipes to investigate the drag reduction behaviors of various polymer solutions, revealing a close correlation between the frictional drag variation of polymer solutions and their viscoelasticity and the extensional viscosity at low shear/strain rates. Donohue et al. [14] performed near-wall dye flow visualization experiments and suggested that polymer additives can alter the structures of the viscous sublayer and near-wall region, thereby influencing the generation of turbulent kinetic energy in wall turbulence. White et al. [15] provided an overview of the research on polymers for turbulent drag reduction, pointing out that high-molecular-weight polymers can achieve drag reduction by altering near-wall turbulent structures, suppressing Reynolds shear stress and regulating turbulent energy dissipation. Motozawa et al. [16] investigated the streamwise process of drag reduction in polymer solutions using particle image velocimetry, revealing that turbulent structures, Reynolds shear stress and wall-normal turbulent intensity undergo significant changes after polymer injection. In the context of hydraulic fracturing, Le Brun et al. [17] studied the drag reduction effectiveness and shear stability of a modified acrylamide copolymer. Habibpour et al. [18] evaluated the turbulent drag reduction performance and shear degradation characteristics of hydrolyzed polyacrylamide (HPAM)/xanthan gum polymer blends using a closed-loop circulation system. Wang et al. [19] and Jing et al. [20,21] investigated the influence of molecular structure,

concentration, and salinity of hydrophobically associating polymers and HPAM with ultra-long side chains using a friction test apparatus.

In terms of weighted fracturing fluids, Qiu et al. [22] and Gupta et al. [23] carried out laboratory evaluations of high-density brine-based fracturing fluids and studied their applications to deep/ultra-deep fracturing, suggesting that weighted systems can decrease the wellhead operating pressure by increasing the hydrostatic pressure. Different weighted systems have been evaluated in terms of density control, crosslinking delay, rheological stability, temperature and shear resistance, and drag reduction, providing an experimental basis for the design of weighted fracturing fluid systems for high-temperature, high-pressure deep reservoirs [5,8,24–26]. Liang et al. [27] proposed a field-scale performance prediction method for drag reducers based on laboratory friction tests, emphasizing the similarity between laboratory parameters (pipe diameter, flow rate, and Reynolds number) and working conditions in the field. These studies indicate that changes in the frictional drag of fracturing fluids are the result of variations in the apparent viscosity of the fluid, as well as the regulating effect of polymers, weighting salt types, and crosslinking structures on near-wall turbulent structures.

Compared with experimental investigations, numerical simulation can capture flow fields and friction characteristics of fracturing fluids in pipes at a lower cost. In direct numerical simulation (DNS) studies, the Navier–Stokes equation is coupled with a viscoelastic constitutive equation to directly resolve the interaction between elastic stress and turbulent structures [28–30]. Oldroyd-B, FENE-P, and Giesekus are commonly used constitutive models [28,29]. Recently, DNS has also been used to research the transition mechanisms of elasto-inertial turbulence and viscoelastic fluids. The findings indicate that polymer elasticity not only weakens conventional inertial turbulence, but also may induce the formation of new elastically unstable structures [31,32]. When DNS is employed, however, all turbulent scales and polymer stress fields have to be resolved, leading to extremely high computational costs. In addition, some parameters of viscoelastic constitutive models such as FENE-P are difficult to obtain directly from experiments. In engineering flow applications, the generalized Newtonian fluid (GNF) model is widely applied to simulate non-Newtonian fluids in pipes, as it can be directly correlated with rheological experimental data. In the GNF model, fluid viscosity is expressed as a function of shear rate, which can be described using the power-law, Cross, or Carreau model [33,34].

In addition to DNS, Reynolds-averaged Navier–Stokes (RANS) and large-eddy simulation (LES) methods are also widely applied to simulate non-Newtonian and viscoelastic fluids, as their computational costs are relatively low. Malin [35] employed the modified k-ε model to investigate the turbulent flow of power-law fluids in pipes, demonstrating that the turbulent model modified with a viscosity function and damping can be used to compute the frictional drag of certain non-Newtonian fluids. Based on the GNF framework, Pinho and Cruz [36,37] developed a low-Reynolds k-ε model suitable for drag-reducing fluids. Furthermore, k-ε-v^2-f, k-ω, and pseudo-elastic stress were modified to improve the ability of RANS to predict turbulent kinetic energy and friction factor [38–40]. Gnambode [41] employed LES to study the turbulent flow of power-law fluids in pipes, suggesting that LES can be used to capture changes in near-wall turbulent structures and the frictional drag of shear-thinning fluids. Amani et al. [42] pointed out that non-Newtonian stress and apparent viscosity fluctuation should not be neglected in the LES of turbulent non-Newtonian fluids. Taghvaei and Amani [43] demonstrated that simulating high-Reynolds pipe flow of non-Newtonian fluids should pursue a balance between accuracy and computational cost. In addition, LES has become an important numerical method for resolving complex turbulent velocity fields and vortex structures. Yang et al. [44] investigated low-speed water entry of a rotating cylinder through experiments and numerical simulations, revealing

how velocity distributions, pressure fields, and vortex structures change under rotational effects. Dai [45] employed LES to study oscillatory flows around a cylinder under high Keulegan–Carpenter and Reynolds number conditions, successfully capturing complex vortex structures and their changes. To sum up, LES can resolve large-scale turbulent structures and deal with small-scale fluctuations using the subgrid-scale model, so it is more suitable for analyzing near-wall turbulent structures and friction-generating mechanisms in non-Newtonian pipe flow.

Previous studies on the friction behaviors of fracturing fluids in pipes have mainly focused on the effects of polymer concentrations, types, and molecular structures. In engineering practice, however, the near-wall turbulent structures and friction behaviors of weighted fracturing fluids in pipes have not been comprehensively investigated, although they may play a crucial role in the design of high-performance weighted fracturing fluids. This study combines rheological experiments, pipe flow friction tests, and three-dimensional numerical simulations of non-Newtonian turbulent flows to investigate the effects of different weighted salt systems on the in-pipe flow field, near-wall turbulent structures, and frictional drag characteristics. Furthermore, the sensitivity of key factors affecting pipe flow friction is analyzed. The results provide theoretical guidance for the optimization of weighted fracturing fluid systems in deep and ultra-deep fracturing operations.

2. Experimental Methodology

2.1. Preparation of Fracturing Fluids

A variety of non-weighted and weighted fracturing fluids were selected as experimental objects for rheological and pipe flow friction experiments. The experimental materials mainly include fresh water, polyacrylamide (PAM), KCl, $CaCl_2$, $CaBr_2$, a temperature stabilizer, a cleanup additive, a demulsifier, and a cosolvent. PAM polymer solutions were used as non-weighted fracturing fluid. Different mass fractions of PAM were added slowly and uniformly to fresh water, which acted as the base fluid, and then stirred continuously for sufficient swell and hydration until the solution was uniform. Following this process, 12 kinds of fracturing fluids with various polymer molecular weights and zero-shear viscosities η_0 were prepared, with polymer molecular weights mainly ranging from 4×10^6 to 9×10^6 and η_0 ranging from 60 to 84 mPa·s. These samples were used to analyze the effect of polymer chain length and zero-shear viscosity on pipe friction.

Four types of weighted fracturing fluids were prepared by adding inorganic salts to water-based fracturing fluids to regulate their density, as shown in Table 1. Weighted fracturing fluid systems are used to investigate the influence of weighting salt type, concentration, and system density on friction behaviors. During the fluid preparation process, weighting salts and fresh water were weighed as per experimental formulations (1 L solution), and then poured into a stirring vessel. A constant-speed stirrer was then started. After the salts were completely dissolved, the relevant additives and polymers were added in succession, while the stirring was maintained to ensure the system was mixed sufficiently. In this way, the corresponding fracturing fluid systems were prepared.

2.2. Pipe Flow Friction Test

The pressure difference method was used to drive the stable flow of fracturing fluids through the test pipe section at a given pipe diameter, pipe length, and flow rate. The inlet pressure and outlet pressure were measured, and their difference was the pressure drop along the pipe section, denoted as ΔP. For engineering applications, since the pressure drop under these conditions is caused solely by frictional resistance at the pipe wall, the pressure drop per unit pipe length, $\Delta P/L$, is more convenient and more commonly used to

characterize variations in frictional resistance. Accordingly, the drag reduction rate, *DR*, can be defined as:

$$DR = \frac{\Delta P_{ref} - \Delta P}{\Delta P_{ref}} \quad (1)$$

where ΔP_{ref} is the corresponding pressure drop of water at the same volume flow rate and in the same pipe. It should be emphasized that *DR* defined in this manner is used primarily as an engineering performance index to quantify the reduction in pumping pressure loss at an identical volumetric throughput.

Table 1. Fracturing fluid formulations.

Fracturing Fluid System	Formulation	Density (kg/m^3)	Zero-Shear Viscosity (mPa·s)
PAM solution	Fresh water +0.5% PAM	1000	60–84
KCl-weighted fracturing fluid	Fresh water + 20% KCl + 0.8% polymer + 0.5% temperature stabilizer + 0.5% cleanup additive + 0.5% demulsifier	1150	30.5
$CaCl_2$-weighted fracturing fluid	Fresh water + 25% $CaCl_2$ + 0.8% polymer + 0.1% cosolvent	1150	42
$CaCl_2$-weighted fracturing fluid	Fresh water + 46% $CaCl_2$ + 0.411% polymer + 0.1% cosolvent	1350	34.5
$CaBr_2$-weighted fracturing fluid	Fresh water + 53% $CaBr_2$ + 0.4% polymer + 0.1% cosolvent	1500	30

Pipe flow friction tests were carried out at 25 °C. A straight pipe with an inner diameter of 12.7 mm and a length of 3 m was used as the test section. The test system consisted of a mixing tank, agitator, screw pump, straight pipe section, flowmeter, pressure sensor, data acquisition system, and waste liquid tank. A sketch of the test system is shown in Figure 1. The prepared fracturing fluids were added to the mixing tank and fluid uniformity was maintained using the agitator, as shown in the photograph of the experimental setup in Figure 2a. The visual control panel was accessed via the computer control system to set up the test pipe diameter, pressure difference range, expected flow rate, sampling frequency, and test time. After parameter setup, the screw pump was started to pump the test fluids from the mixing tank to the straight pipe section. Data recording began when the flow rate became stable. A flowmeter was used to monitor the inlet flow rate in real time, as shown in the photo in Figure 2b. During the tests, the flow rate was initially 10 L/min and then increased at the rate of 5 L/min until the highest value of 90 L/min was reached. The corresponding pressure difference was recorded after the flow rate became stable. The flow rate, pressure difference, and temperature were recorded synchronously using the data acquisition system. After each sample test, the system was cleaned before testing the next sample. Upon completion of all tests, the experimental data were exported to calculate the frictional drag and *DR* of the fracturing fluids in the pipes.

2.3. Rheological Test

Fracturing fluids are non-Newtonian fluids whose viscosity is not constant but varies with shear rate. Therefore, zero-shear viscosity alone cannot accurately describe the actual rheological behavior of fracturing fluids during high-shear flow in pipes. To support the pipe flow friction tests, steady-state shear tests were conducted to characterize the rheological behavior of fracturing fluids and the variation in apparent viscosity over a range of shear rates. During the test, the rheometer applies shear force to samples by rotating the rotator and records the stress response of each sample. In principle, it converts

the angular displacement and velocity of motor rotation into strain and shear rate, and the measured torque into shear stress. The apparent viscosity of samples at various shear rates can be calculated based on the relationship between shear stress and shear rate, as shown in Equation (2).

$$\eta = \frac{\tau}{\dot{\gamma}} \tag{2}$$

where η is the apparent viscosity in Pa·s, τ is the shear stress in Pa, and γ is the shear rate in s^{-1}.

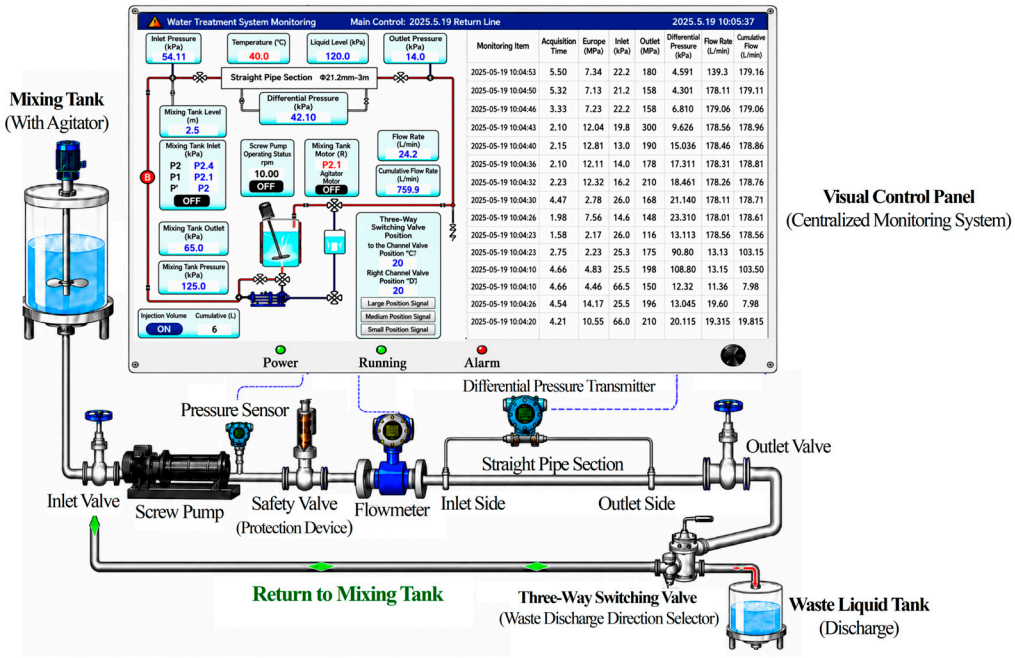
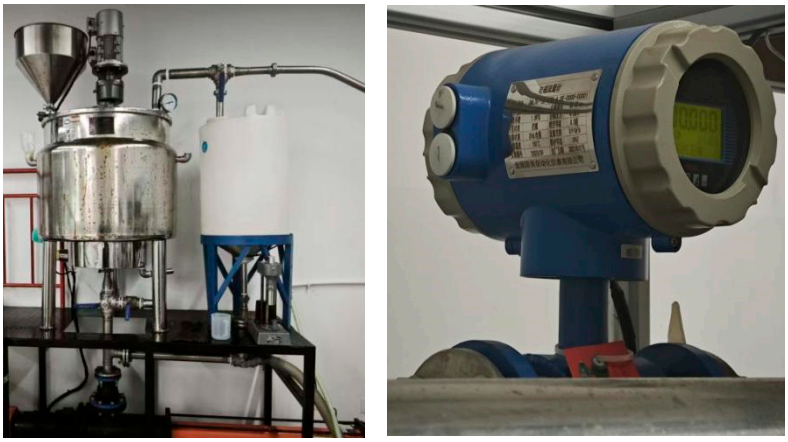


Figure 1. Schematic test system.



(**a**) Mixing tank (with agitator) (**b**) Flowmeter

Figure 2. Schematic test devices.

A Thermo Scientific HAAKE MARS60 rotational rheometer (Thermo Scientific, Karlsruhe, Germany) and its supporting control system were employed, as shown in Figure 3. Before testing, the air compressor and host rheometer were started, and the temperature control system and measurement rotator were confirmed to be normal. The steady-state shear test procedure was established according to the experimental plan using HAAKE RheoWin software (4.41.0019), with the shear rate ranging from 0.1 to 1000 s^{-1} and the test temperature maintained at a constant value. Multiple data points were acquired continu-

ously, and their average was taken as the η at each level of shear rate. After all samples were tested, the shear rate, shear stress, and η data were output, and the measurement system was cleaned.



Figure 3. MARS60 rotary rheometer and its supporting control system.

3. Numerical Simulation Methods

3.1. Governing Equations

It is assumed that the flow of fracturing fluids in a cylindrical pipe is three-dimensional, transient, and incompressible, and that the fluid density ρ remains constant. The continuity equation and momentum equation are

$$\nabla \cdot \mathbf{u} = 0 \tag{3}$$

and

$$\frac{\partial \mathbf{u}}{\partial t} + \nabla \cdot (\mathbf{u} \otimes \mathbf{u}) = -\frac{1}{\rho}\nabla p + \nabla \cdot \tau \tag{4}$$

where $\mathbf{u}$ is the velocity vector in m/s, p is the static pressure in Pa, τ is the viscous stress tensor, and ρ is the density in kg/m^3.

Considering that DNS has excessively high computational costs and the RANS method struggles to resolve near-wall turbulent fluctuations, which may affect the prediction accuracy of frictional resistance at medium Reynolds numbers, this study employs the LES method in numerical simulation and applies the finite volume method to spatial discretization. In LES, turbulent motion is decomposed through spatial filtering into large-scale analyzable structures and small-scale non-analyzable fluctuations. Large-scale eddies are solved directly via governing equations, while the influence of small-scale eddies is enclosed with a subgrid-scale (SGS) model. In this study, the Wall Adaptive Local Eddy (WALE) viscosity model [46] was selected as the SGS model, which can reasonably describe the attenuation characteristics of eddy viscosity near the wall and is suitable for turbulent flow constrained by the inner pipe wall. A second-order upwind scheme and second-order discretization are used for the discretization of the momentum equation and pressure field. The second-order implicit method is adopted for time discretization. Pressure-velocity coupling is handled using a coupled algorithm.

3.2. Rheological Model

Tests of weighted fracturing fluids for engineering practice indicate that their viscosity varies with strain rate. In this study, the generalized Newtonian fluid (GNF) constitutive model was employed to describe the viscous stress tensor of the fluids. Unlike Newtonian

fluids, the apparent viscosity in the GNF model is not a constant but a function of shear rate. Therefore, the viscous stress tensor can be expressed as follows:

$$\tau = 2\mu(\dot{\gamma})D \tag{5}$$

where $\mu(\dot{\gamma})$ is the viscosity function, D is the strain rate tensor, which is defined as

$$D = \frac{1}{2}\left[\nabla \mathbf{u} + (\nabla \mathbf{u})^T\right] \tag{6}$$

and $\dot{\gamma}$ is the shear rate, expressed as $\dot{\gamma} = \sqrt{2D : D}$. Therefore, the viscous stress tensor in the GNF model can be expressed as

$$\tau = \mu(\dot{\gamma})\left[\nabla \mathbf{u} + (\nabla \mathbf{u})^T\right] \tag{7}$$

In the Power-Law model, the viscosity function is

$$\mu(\dot{\gamma}) = K\dot{\gamma}^{n-1} \tag{8}$$

where K is the consistency coefficient, representing the measurement of fluid viscosity at unit shear rate, and n is the rheological index, determining the deviation degree and direction of fluid from Newtonian behavior: $n < 1$ indicates shear thinning, while $n > 1$ indicates shear thickening.

It should be particularly noted that the generalized Newtonian power-law model employed in this study describes the shear-thinning behavior of the fluid through shear-rate-dependent apparent viscosity. Its constitutive relation does not include polymer extra stress, relaxation time, finite extensibility, or molecular conformation. Therefore, this model cannot reproduce the classical Toms drag-reduction effect arising from the interaction between polymer elastic stresses and turbulence. The LES results presented in this study are used only to analyze the effects of shear-thinning rheological behavior on pipe-flow friction and turbulent structures.

3.3. Computational Domains and Boundary Conditions

To investigate the turbulent frictional behavior of shear-thinning fracturing fluids in circular pipes, a computational domain for numerical simulation was established with reference to the experimental model dimensions reported by Sorgun et al. [47], as shown in Figure 4. A cylindrical coordinate system was adopted, in which z, r, and θ represent the axial flow direction, wall-normal direction, and circumferential direction, respectively. Periodic boundary conditions were applied in the streamwise direction to obtain a stable and fully developed pipe flow within a relatively short computational domain. Because the pipe diameter and flow conditions vary among the simulated cases, the absolute streamwise length of the computational domain is not fixed. For each case, the streamwise length L_z is determined according to Equation (9) to satisfy the minimum domain-length requirement for fully developed turbulent flow. The finite computational domain represents a periodically repeated section of fully developed pipe flow rather than the total physical pipe length.

$$L_z = C \times \frac{\mu}{\rho u_\tau} \tag{9}$$

where L_z is the streamwise length of the computational domain in m, C is set to 2000 based on experience, μ is the viscosity in Pa·s, ρ is the density in kg/m^3, u_τ is the friction velocity, calculated by $u_\tau = \sqrt{\tau_\omega/\rho}$ in m/s, and τ_w is the wall shear stress in Pa.

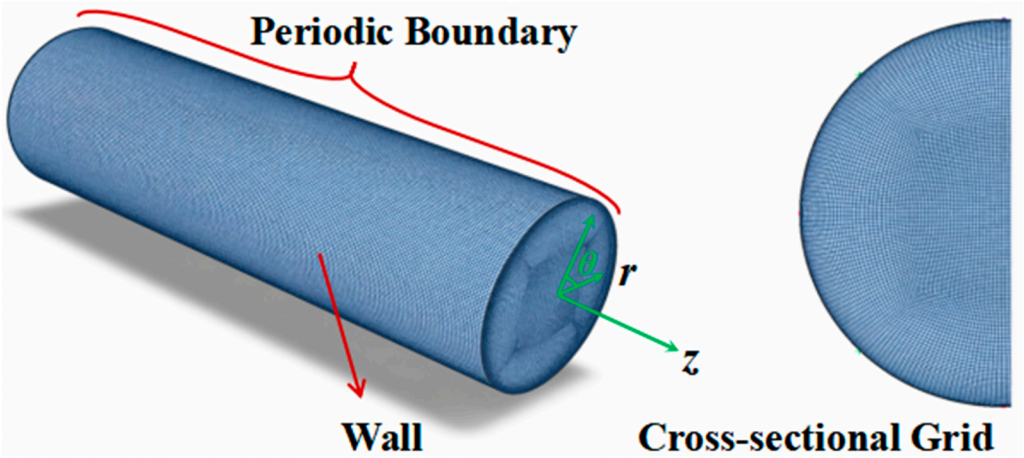


Figure 4. Schematic computational domain.

The non-slip boundary conditions were applied to the wall, without considering the influence of wall roughness and gravity. A structured hexahedral grid was employed for spatial discretization. The meshes in the streamwise and circumferential directions (r and θ) are divided uniformly. The O-grid division method is used in the wall-normal direction. To evaluate the influence of grid scale on computational results and determine the optimal grid distribution that meets the required computational accuracy, a grid independence study was conducted. LES calculations were performed under the same flow conditions using four grid resolutions, denoted as M_1, M_2, M_3, and M_4. The detailed grid sizes and corresponding results are summarized in Table 2.

Table 2. Mesh configurations and friction-factor results for the grid-independence study.

Case	Grid Number	Δz^+	$\Delta r^+{}_{\min}$	$\Delta r^+{}_{\max}$	Colebrook Prediction, f	f_{LES}	Δf_{LES}
M_1	1.07×10^6	15	0.8	15	0.0076	0.00719	5.39%
M_2	1.61×10^6	15	0.8	10	0.0076	0.00735	3.29%
M_3	3.52×10^6	10	0.8	10	0.0076	0.00756	0.53%
M_4	6.18×10^6	8	0.8	10	0.0076	0.00756	0.53%

The Fanning friction factor, f, is defined as

$$f = \frac{\tau_w}{1/2\rho U^2} \tag{10}$$

where τ_w is the wall shear stress in Pa, ρ is the fluid density, and U is the bulk mean velocity. The relative error is defined as $\Delta f = |f - f_{pred}|/f_{pred} \times 100\%$, where f_{pred} denotes the Fanning friction factor predicted by the Colebrook equation.

The radially averaged dimensionless velocity profiles obtained with the four grid resolutions were compared with the DNS results reported in reference [48], as shown in Figure 5. Near-wall refinement was applied to all four grids, with the first-wall grid spacing satisfying ${r_{\min}}^+ < 1$, the radial grid scale $\Delta {r_{\max}}^+ \leq 10$, and the streamwise and circumferential grid scales $\Delta z^+ \leq 10$ and $\Delta(r\theta)^+ \leq 10$, where the superscript "+" represents the result normalized by the wall unit. The comparison results demonstrate that the computational grids have met the requirement of grid independence. The selection ranges for the key parameters used in the simulation are shown in Table 3.

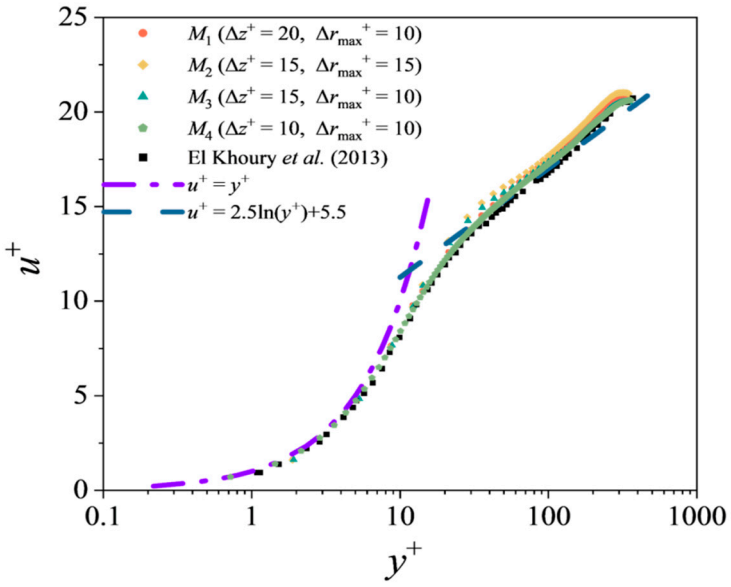


Figure 5. Comparison between the averaged velocity along the wall normal and DNS results [48].

Table 3. Selected ranges of key parameters used in the simulations.

Flow Rate, Q	Diameter, D	Density, ρ	Consistency Parameter, K	Power-Law Index, n
110~430 L min^{-1}	35~100 mm	1100~1400 kg m^{-3}	0.04~0.302	0.55~0.85

A user-defined function is established for the obtained apparent viscosity, enabling the viscosity to be updated in real time according to the shear rates during the computation process, to fully capture the shear rheological behaviors of weighted fracturing fluids. To accelerate convergence and ensure comparability among different cases, a Newtonian-fluid LES was first performed at the corresponding Reynolds number to reach a statistically stationary turbulent state, which was then used as the initial condition for the corresponding non-Newtonian LES to preserve a well-developed initial turbulent structure. The statistics of the non-Newtonian LES were collected over approximately five flow-through times after statistical stationarity was achieved. The maximum time step for the LES calculations should satisfy $\Delta t \leq \Delta z/U_z$, where U_z is the characteristic streamwise velocity and Δz is the physical streamwise grid spacing. Because the characteristic streamwise velocity and the physical streamwise grid spacing differed among the numerical simulation cases, different time-step sizes were adopted for different cases. For example, when D = 0.035 m, Q = 430 L/min, and L_z = 0.021 m, a time step of 1×10^{-6} s was used. When D = 0.06 m, Q = 320 L/min, and L_z = 0.1 m, a time step of 6×10^{-5} s was used. Considering all numerical simulation cases investigated in this study, the time-step size ranged from 1×10^{-6} to 1×10^{-4} s. The computation is considered to be converged when the residuals of all variables in the simulation equations drop below 10^{-5}.

3.4. Validation of Numerical Model

The complexity and uncertainty inherent in the experimental data of coiled tubing hinder their direct application to the validation of numerical simulation results. Thus, we adopt the experimental data from Sorgun et al. [47], who used similar fluid properties and flow conditions to validate the numerical method, as shown in Figure 6. The corresponding dimensionless generalized Reynolds number ($Re_g = \rho U^{2-n} D^n/(K8^{n-1})$, where Re_g is the dimensionless generalized Reynolds number, U is the bulk mean velocity in m/s, and D is the pipe diameter in m) ranges from 3600 to 4600. This indicates that the numerical

simulation results are overall in good agreement with the experimental data, with an average relative deviation of about 10% and a minimum of around 5%. From an engineering perspective, the above discrepancy is within the acceptable range, indicating that the current method can reasonably predict the pipe-flow friction of shear-thinning fluids. It should be noted that the discrepancies are mainly induced by the GNF model. Despite this, the present results are generally consistent with the recent findings in reference [49], suggesting the good applicability of this model.

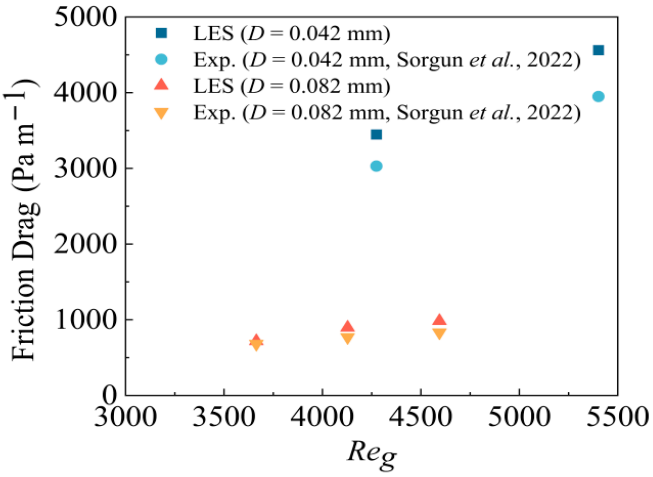


Figure 6. Comparison of frictional drag between numerical results and experimental results of pipes with diameters of 42 mm and 82 mm [47].

It should be noted that all simulated conditions are within the turbulent regime. Figure 7 shows a comparison of the axial and radial root-mean-square fluctuating velocities $u_{rms}{}^{+}$ and $v_{rms}{}^{+}$ along the wall-normal direction between the LES results and the DNS data [48]. The distribution of $u_{rms}{}^{+}$ for power-law fluids is generally consistent with the DNS results, except for some discrepancies near the peak and in the outer layer. The radial velocity fluctuations of power-law fluids are obviously affected by rheological behaviors and exhibit differences from the DNS data. At a moderate Reynolds number of 4128, $v_{rms}{}^{+}$ exhibits weaker turbulent fluctuations and characteristics of early turbulence. The employed numerical method demonstrates good capability for predicting turbulent statistics in pipes.

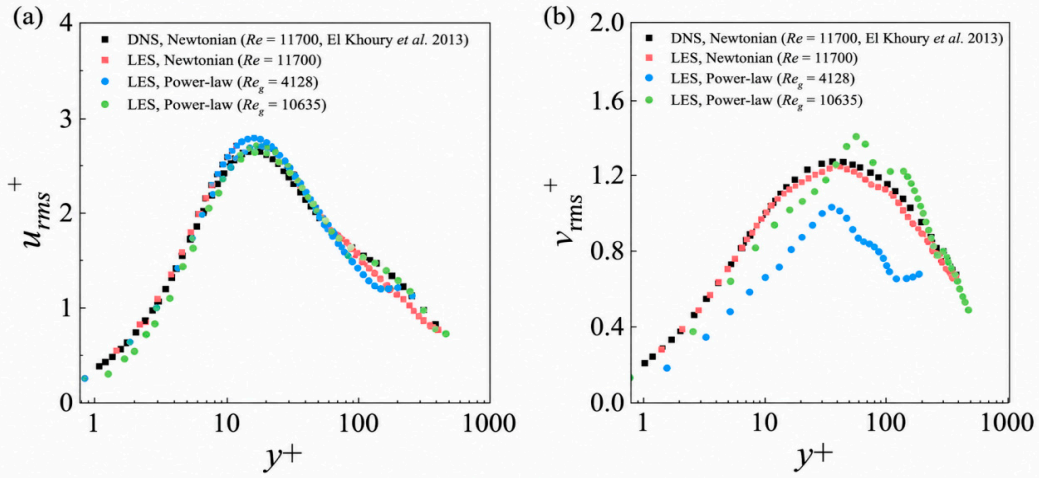


Figure 7. Comparison of dimensionless Reynolds stress (**a**) $u_{rms}{}^{+}$ and (**b**) $v_{rms}{}^{+}$ under various flow conditions and DNS result [48].

4. Results and Discussions

4.1. Friction Characteristics of Fracturing Fluids

The generalized Reynolds number Re_g was calculated for each experimental condition based on the corresponding rheological parameters and flow rate. For the non-weighted PAM solutions, Re_g ranges from approximately 3000 to 15,000 for $Q \geq 30$ L/min, whereas for the weighted fracturing fluids, the corresponding range is approximately 3100–18,000. Experimental cases below 30 L/min do not reach a fully turbulent state. These low-flow-rate data are retained to illustrate the complete evolution of pressure drop and drag-reduction rate with flow rate, whereas the discussion of turbulent frictional behavior is primarily based on the cases with $Q \geq 30$ L/min.

(1) Friction characteristics of non-weighted fracturing fluids

The pressure drop data for 12 kinds of PAM solutions at various flow rates were acquired and compared with the results for fresh water. To ensure comparability among different experimental cases, a control-variable strategy was adopted for the pipe-flow experiments. To evaluate the reproducibility and experimental uncertainty of the PAM solution friction measurements, the friction tests for each PAM solution were independently repeated three times under the same operating conditions. When preparing PAM solutions with different molecular weights, the PAM concentration was adjusted to maintain the same zero-shear viscosity (η_0 = 84 mPa·s). The corresponding concentrations of PAM solutions with molecular weights of 400–500 × 10^4, 500–600 × 10^4, 600–700 × 10^4, and 800–900 × 10^4 were 0.67%, 0.65%, 0.60%, and 0.57%, respectively. Figure 8 illustrates the variations in frictional pressure drop and drag reduction rate of PAM solutions with different molecular weights under the same zero-shear viscosity condition (η_0 = 84 mPa·s). As the flow rate increases from 10 to 90 L/min, the pressure differences of fresh water and PAM solutions all increase gradually, and the frictional drag along the pipe increases. Compared with fresh water, PAM polymer solutions have a slower increase in pressure difference. At the low flow rate stage (10–30 L/min), the frictional pressure drop of PAM solutions is larger than that of fresh water. It indicates that polymer viscosity resistance is dominant, and the drag increases. When the flow rate exceeds 30 L/min, the frictional pressure drop of PAM solutions is smaller than that of fresh water; the drag reduction rate transforms from negative to positive, indicating that drag reduction occurs. As the flow rate increases, the drag reduction rate increases continuously, which may be attributed to both shear-thinning behavior and the viscoelastic properties of the polymer.

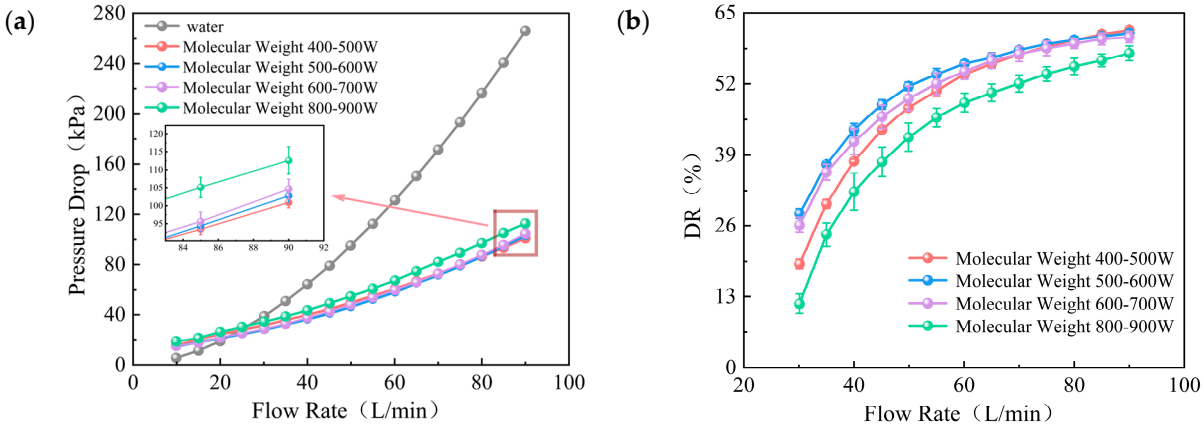


Figure 8. Variation in the (**a**) pressure drops and (**b**) DRs of PAM solutions with various molecular weights at different flow rates.

Regarding the influence of molecular weights, PAM solutions are basically consistent in the pressure drop variation trend at the identical zero-shear viscosity, but differ in drag reduction effectiveness at high flow rates. The PAM solutions with small or medium molecular weights have relatively low frictional drag, with a maximum drag reduction rate of up to 62%, while those with molecular weights of 800 × 10^4 to 900 × 10^4 have relatively high frictional pressure drops, with a maximum drag reduction rate of 56%. The polymer concentration required to maintain the same zero-shear viscosity (η_0 = 84 mPa·s) gradually decreased with increasing PAM molecular weight. Consequently, the number of effective polymer chains per unit volume in the higher-molecular-weight systems was reduced, which may weaken the overall interaction between the polymer molecules and turbulent structures. In addition, longer PAM chains may be more susceptible to mechanical degradation under high-shear turbulent conditions, thereby reducing their effective molecular weight and drag-reduction capability. Therefore, under the present experimental conditions, an excessively high molecular weight did not further improve the drag-reduction performance, whereas PAM with an intermediate molecular weight exhibited better overall drag-reduction efficiency.

While maintaining the PAM molecular weight within the range of 600–700 × 10^4, three PAM solutions with η_0 values of 60, 66, and 84 mPa·s were prepared by adjusting the polymer concentration to approximately 0.55%, 0.57%, and 0.60%, respectively. Figure 9 shows the variation in the pressure drop and *DR* of PAM solutions with η_0. PAM solutions with various η_0 values all exhibit increasing *DR* with increasing flow rate. At low flow rates, *DR* is relatively low, and with increasing flow rates, it increases rapidly. At high flow rates, the *DR*s of PAM solutions increase slowly and gradually approach stability, with the maximum value ranging from 60% to 62%. The PAM solution with η_0 = 60 mPa·s exhibits the lowest pressure drop and the highest *DR*, while that with η_0 = 84 mPa·s exhibits an opposite trend This may be attributed to the increased viscous resistance of the fluid associated with higher PAM concentration and zero-shear viscosity, which may partially weaken the drag-reduction effect. Therefore, under the present experimental conditions, appropriately reducing the zero-shear viscosity may lead to better drag-reduction performance.

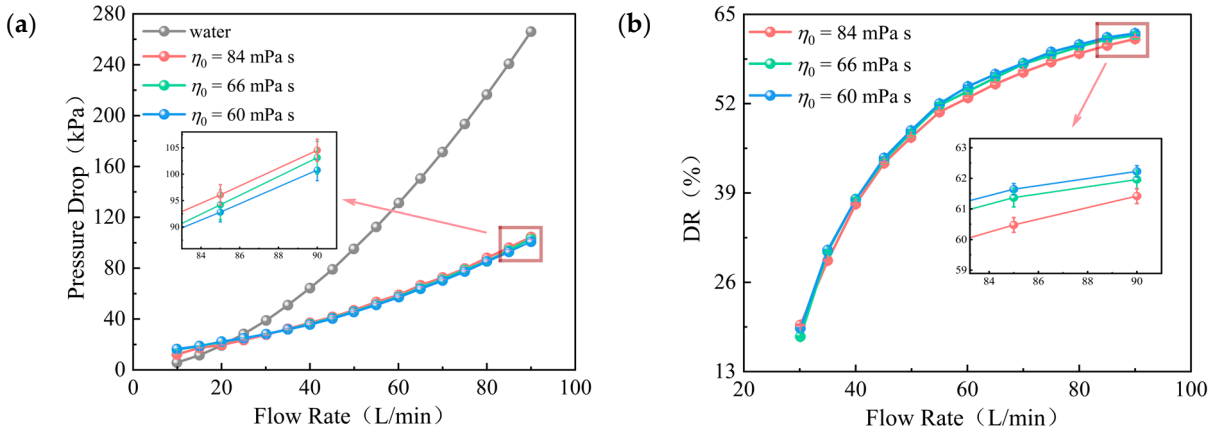


Figure 9. Variation in the (**a**) pressure drops and (**b**) *DR*s of PAM solutions with different zero-shear viscosities at different flow rates.

(2) Friction characteristics of weighted fracturing fluids

The pressure drops of four types of weighted fracturing fluids at various flow rates were acquired in the friction experiments and compared with fresh water results to calculate the *DR* of each formulation system. The densities of weighted fracturing fluids are 1150 kg/m^3, 1150 kg/m^3, 1350 kg/m^3, and 1500 kg/m^3, respectively. To evaluate

the reproducibility and uncertainty of the experimental results, the friction tests for each weighted fracturing fluid were independently repeated three times under the same operating conditions. Figure 10 shows the variation in the pressure drops and *DR*s of each system with flow rate, which are reported as the mean values of three repeated measurements, and the error bars represent one standard deviation (mean ± SD, n = 3). Even though their pressure drops increase with flow rate, the four types of weighted systems still exhibit certain drag reduction behaviors compared with fresh water. At the maximum flow rate of 90 L/min, the *DR*s of the 20% KCl, 25% $CaCl_2$, 46% $CaCl_2$, and 53% $CaBr_2$ systems are 64.77%, 57.72%, 49.36%, and 42.29%, respectively. Among these formulations, the 20% KCl system has the smallest pressure drop, and the 53% $CaBr_2$ system has the largest one. This indicates that, from the perspective of drag reduction effectiveness, the KCl system is the best, followed by the $CaCl_2$ system, and the $CaBr_2$ system is the worst. The four weighted systems differ not only in the type and concentration of weighting salts, but also in fluid density and polymer dosage. Therefore, the above experimental ranking should be interpreted as the result of the combined effects of the different formulation factors.

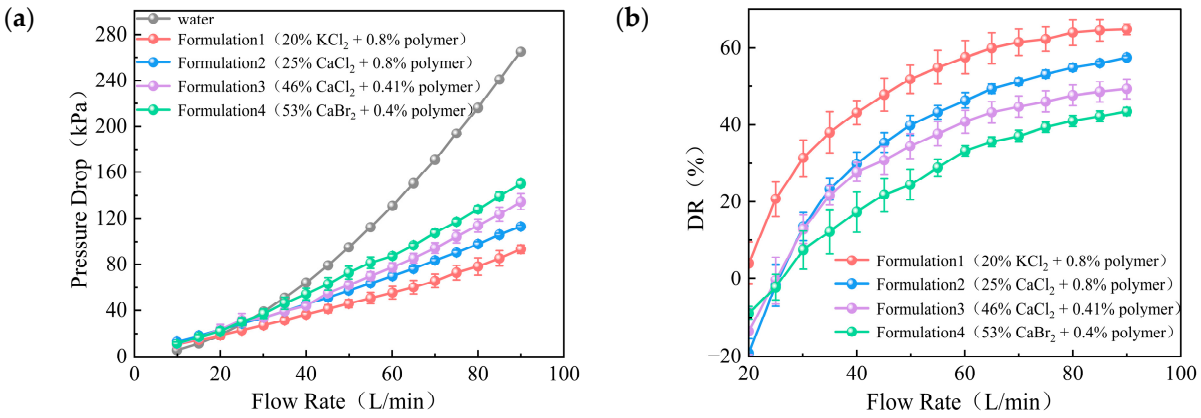


Figure 10. Variation in the (**a**) frictional pressure drops and (**b**) *DR*s of various fracturing fluid formulations at different flow rates.

It is worth noting that, although some weighted fracturing fluids exhibit lower drag reduction performance than non-weighted PAM solutions, their higher fluid density increases the hydrostatic pressure in the wellbore, thereby reducing the wellhead pump pressure required to achieve the same bottomhole pressure. For a given well depth, when the target bottomhole pressure P_{bh} remains constant, the required wellhead pump pressure can be approximately expressed as

$$P_{surface} = P_{bh} - \rho g H + \Delta P_f \tag{11}$$

where P_{bh} is the bottomhole pressure, $\rho g H$ is the hydrostatic pressure, and ΔP_f is the frictional pressure loss along the wellbore. Taking the non-weighted PAM solution with a density of approximately 1000 kg/m^3 as the reference, a weighted fracturing fluid with a density of 1350 kg/m^3 provides an additional hydrostatic pressure of approximately 3.43 MPa for every 1000 m of vertical fluid column. Therefore, as the fluid density increases, a larger portion of the required bottomhole pressure is provided by the fluid column itself, thereby reducing the pressure that must be supplied by the surface pumps.

It should be noted that the above discussion involving molecular-chain conformation, entanglement, hydration, and stretching behavior is primarily intended to interpret the observed experimental trends based on the general physical characteristics of polymer solutions, rather than to serve as direct evidence of the specific molecular mechanisms involved.

4.2. Rheological Characteristics of Fracturing Fluids

(1) Rheological characteristics of non-weighted fracturing fluids

Figure 11 shows the variations in apparent viscosity of different PAM solutions at various shear rates. All 12 samples exhibit obvious shear-thinning behavior. At low shear rates of 0.1–1 s^{-1}, the apparent viscosity η remains relatively high, indicating strong polymer chain entanglement and significant structural resistance within the solution. As the shear rate increases gradually, the entanglement degree of polymer molecular chains decreases, and η drops rapidly. When the shear rate reaches the intermediate-to-high range of 10–500 s^{-1}, the decrease in viscosity becomes less pronounced. When the shear rates reach 500–1000 s^{-1}, the viscosity of most samples gradually approaches a stable value.

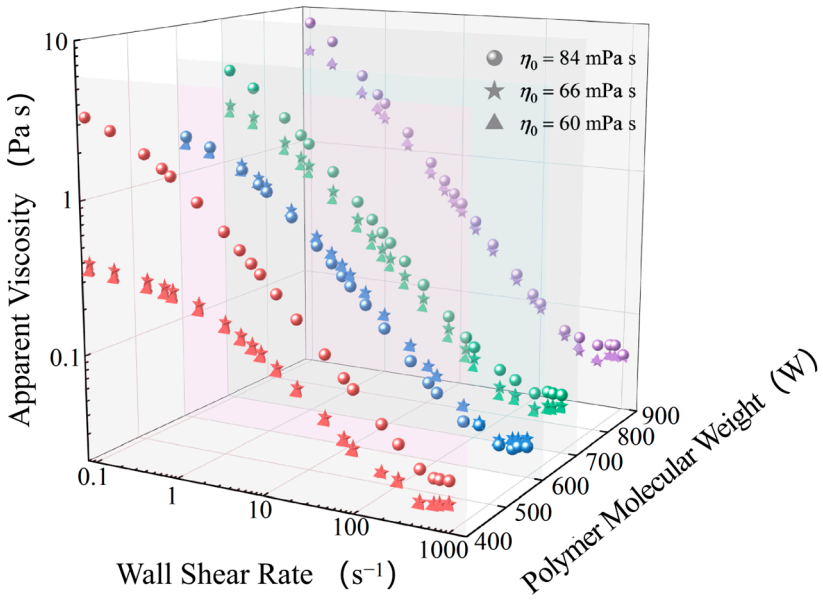


Figure 11. Variation in the apparent viscosities of PAM samples at different shear rates, colors indicate different polymer molecular weights.

The sample comparison results indicate that the samples with higher zero-shear viscosity have higher η values. At low shear rates, the samples with η_0 = 84 mPa·s exhibit the highest viscosity, followed by those with η_0 = 66 mPa·s and η_0 = 60 mPa·s. Furthermore, as the molecular weight of PAM increases, the η of the solution increases overall, indicating that the PAM with a larger molecular weight has a stronger viscosity-enhancing ability and a greater degree of molecular chain entanglement. At high shear rates, however, the viscosities among different samples tend to be consistent, indicating that strong shear effect can mitigate the influence of η_0 and molecular weight on η.

This rheological behavior is consistent with the friction test results. At low flow rates, the shear effect in pipes is weak, and the PAM solution maintains a high η, so viscous resistance performs as a dominant factor. Some samples may exhibit low drag reduction rates. Nevertheless, the contribution of viscoelastic effects in the polymer solution to the experimentally observed drag reduction cannot be neglected. As the flow rate rises, the average flow velocity and wall shear rate in the pipe increase, and the PAM solution undergoes shear thinning, thereby reducing the flow resistance. Consequently, the pressure difference is lower than that of fresh water, and the drag reduction rate gradually increases and tends to stabilize.

(2) Rheological characteristics of weighted fracturing fluids

Figure 12 shows the apparent viscosity of four types of weighted fracturing fluids at varying wall shear rates. All of these weighted fracturing fluids present certain shear-thinning characteristics. At low shear rates, the initial η of weighted fracturing fluids is lower than that of non-weighted PAM solutions. As the shear rates increase, the viscosity of all systems decreases to relatively low levels at moderate shear rates.

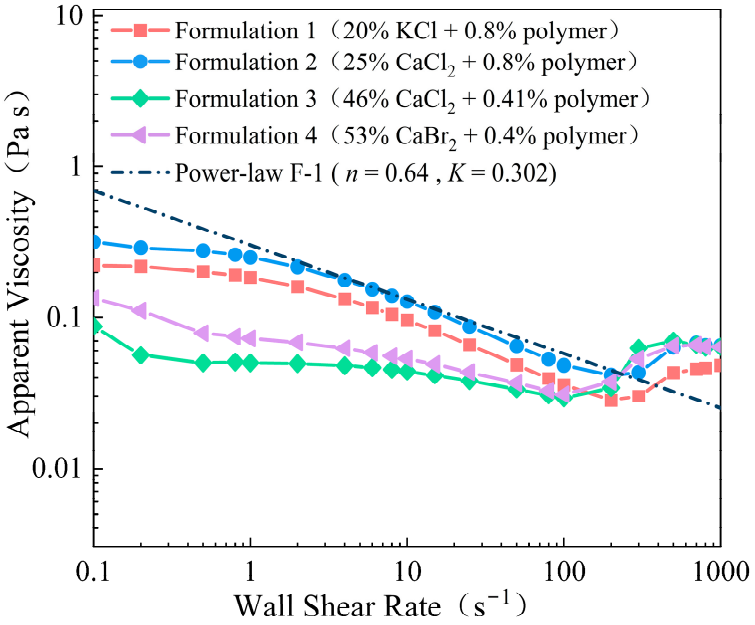


Figure 12. Rheological behaviors of weighted fracturing fluids and F-1 fluid [47].

The formation comparison results show that formulations 1 and 2 have higher polymer content, and their apparent viscosities are overall higher than those of formulations 3 and 4. As the shear rates increase, the viscosity differences among these formulations decrease gradually. This indicates that a strong shear effect mitigates the influence of polymer concentration and weighting salt type on η. It should be noted that at high shear rates of 500–1000 s^{-1}, the apparent viscosity of the weighted fracturing fluids no longer decreases continuously, but exhibits a slight increase or fluctuation. This behavior may reflect a complex high-shear response of the polymer–salt systems; however, possible experimental effects, such as instrumental inertia, temperature rise, edge effects, and wall slip, may also contribute to the observed viscosity variation.

In addition, the power-law fluid F-1 used for numerical model validation is also shown in Figure 12. A comparison of the rheological behavior of the four weighted fracturing fluid formulations with that of the F-1 fluid indicates that the viscosity of the F-1 fluid generally falls within the curve range of the actual fracturing fluids, confirming comparability between the numerical simulation and the experiments.

4.3. Average Axial Velocity

For the parametric LES analysis, fluid density ρ, pipe diameter D, consistency coefficient K, power-law index n, and flow rate Q were varied independently, while the remaining parameters were maintained at their corresponding baseline values. Re_g ranges approximately from 3500 to 53,000, corresponding to turbulent pipe-flow conditions.

Figure 13 shows the average axial velocity profiles normalized by the friction velocity for different densities, pipe diameters, K values, and n values. All profiles exhibit typical turbulent velocity distribution characteristics, with the velocity increasing rapidly in the near-wall region and then increasing more gradually beyond the buffer layer. As the fluid density increases from 1009.6 kg/m^3 to 1400 kg/m^3 in Figure 13a, the velocity profiles tend

to shift upward in the logarithmic and outer layers, while remaining almost unchanged in the near-wall viscous region. Under the same flow conditions, an increase in density enhances liquid inertia and thus the turbulent momentum transport, leading to an increase in axial velocity in the outer layer. As the pipe diameter increases from 35 mm to 100 mm in Figure 13b, the dimensionless axial velocity exhibits a decreasing trend after entering the buffer layer and the logarithmic layer. With increasing pipe diameter, the flow scale increases, while the wall shear effect on the fluid weakens, resulting in a change in the velocity gradient and consequently a downward shift of the velocity profile. As the consistency coefficient K increases from 0.04 to 0.3 in Figure 13c, the velocity profiles overall exhibit a slight descending trend. The consistency coefficient K reflects the viscous resistance level of fluids, and its increase results in a higher η under the same shear conditions, which enhances the viscous dissipation effect during the flow process, thereby reducing the momentum transport capacity of fluids and shifting the velocity profiles downward. As n increases from 0.55 to 0.85 in Figure 13d, the velocity profile gradually shifts downward, with a lower n corresponding to a higher dimensionless axial velocity. This is because n characterizes the degree of shear thinning of the fluid. As n decreases, the non-Newtonian shear-thinning effect becomes more pronounced, reducing η and the flow resistance in the near-wall region where the shear rate is high. Consequently, less momentum is dissipated, resulting in an upward shift of the velocity profile.

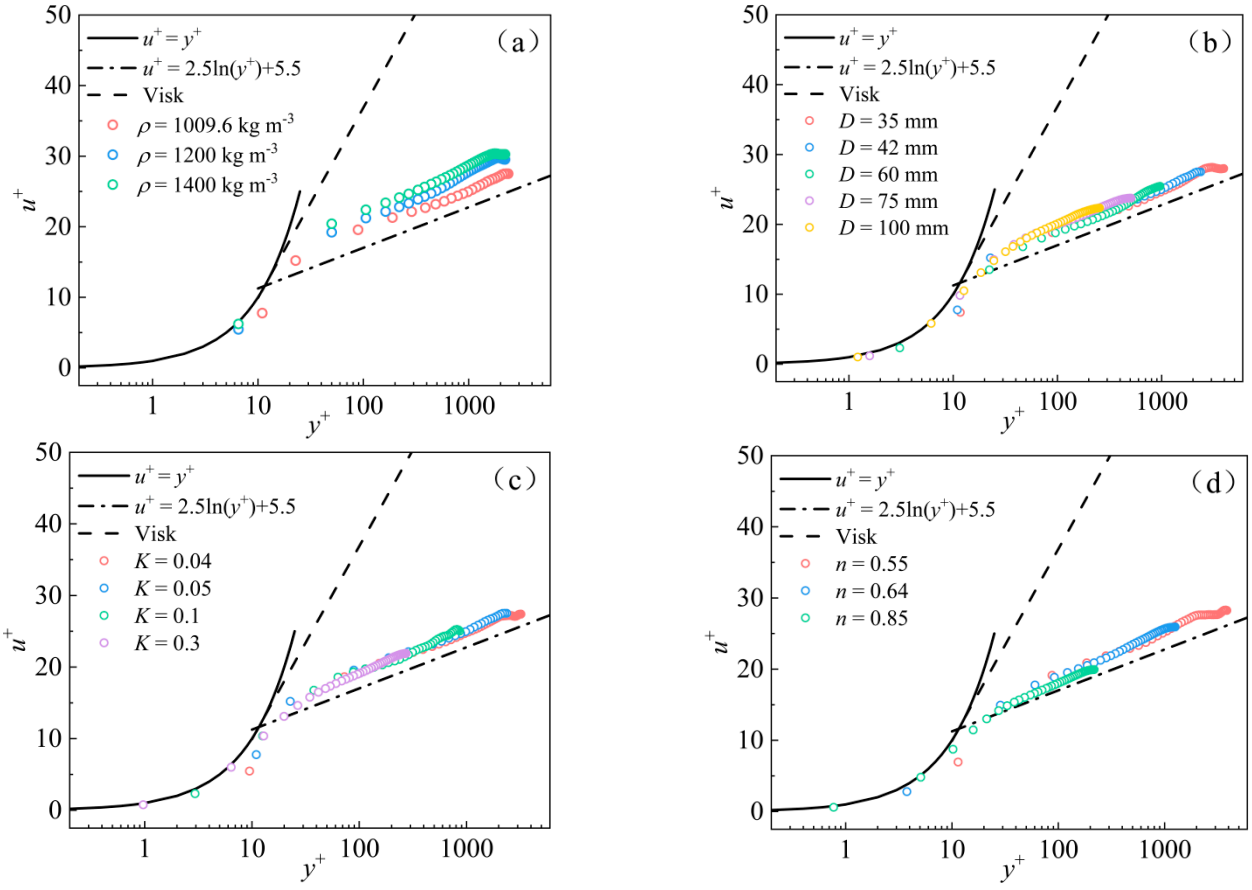


Figure 13. Average axial velocities for different (**a**) densities, (**b**) pipe diameters, (**c**) K values, and (**d**) n values.

4.4. Flow Field Analysis

The influences of flow conditions and physical property parameters on the turbulent structures of weighted fracturing fluids in pipes were investigated and analyzed. The

power-law index n directly characterizes the fluid shear-thinning behaviors, and its variation has a more significant impact on the turbulent structure and velocity distribution than other parameters. Therefore, n was selected as a representative parameter, and the flow fields at n = 0.85 and 0.55 were analyzed.

Figure 14 shows the cross-sectional contour of streamwise velocity near the wall (x = −0.0209 m) at a flow rate of 320 L min^{-1}. At n = 0.85, the overall velocity near the wall is relatively low, the high-velocity core region occupies a small area, and the streaky structures are dispersed and discontinuous, corresponding to a low shear rate. Based on the vortices identified by Q criterion isosurfaces and colored by velocity values shown in Figure 15, a relatively large low-velocity region exists near the wall at n = 0.85, and the turbulent structures in the flow field are large in scale and relatively regular in spatial distribution. Furthermore, the flow vorticity contours on the cross-section were compared, as shown in Figure 16. At n = 0.85, the vortices are mainly distributed near the wall, and the vortex intensity is relatively low, indicating weak turbulent energy dissipation. With a higher apparent viscosity at the wall, viscous energy dissipation is enhanced. The DR results indicate that the latter effect plays a dominant role in this case, leading to increased friction drag. At n = 0.55, the near-wall velocity is generally higher, as shown in Figure 14; the high-velocity core region occupies a larger area, and the streaky structures are longer and more continuous. As shown in Figure 15, the high-velocity region extends from the pipe center toward the wall, accompanied by increases in the velocity gradient and near-wall velocity. Meanwhile, the turbulent structures in the flow field are smaller in scale and randomly distributed. As shown in Figure 16, the vortices extend from the near-wall region toward the center of the pipe, with relatively intense vorticity fluctuations and higher vortex intensity near the wall. These features indicate that the fluid has developed into a typical turbulent region with pronounced turbulent effects. The near-wall shear rate is higher, and the apparent viscosity decreases, which significantly reduces the frictional drag.

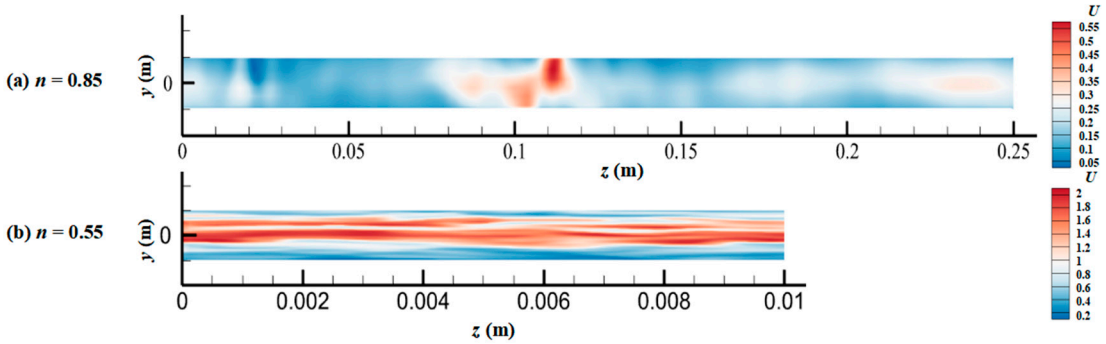


Figure 14. Velocity contour near the wall at x = −0.0209 m at (**a**) n = 0.85 and (**b**) n = 0.55.

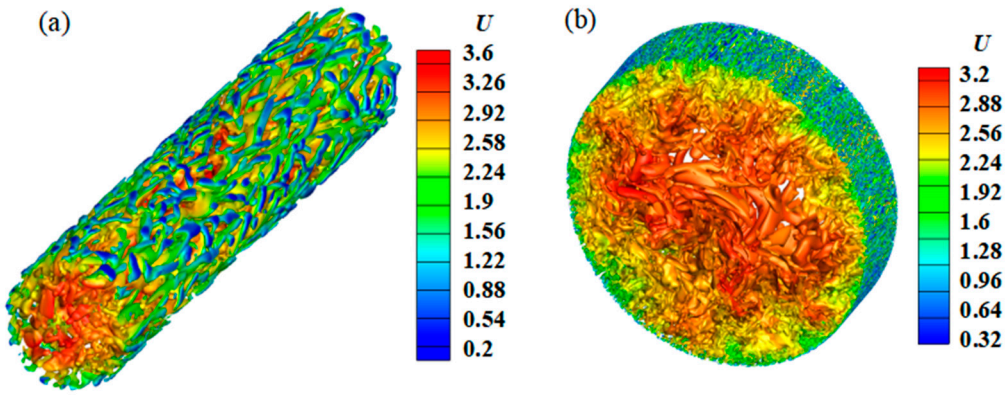


Figure 15. Q criterion isosurfaces colored by velocity values at (**a**) n = 0.85 and (**b**) n = 0.55.

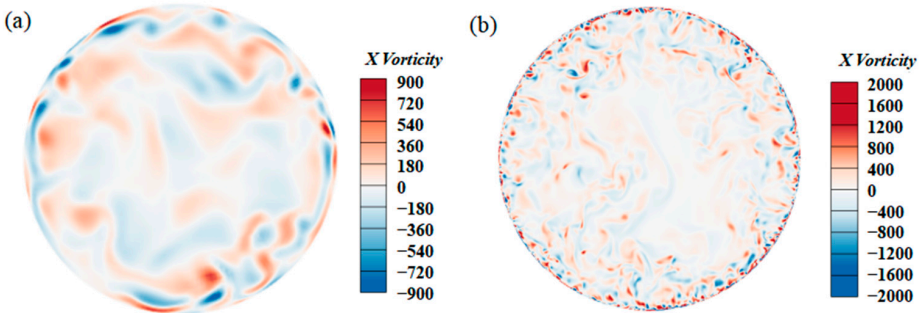


Figure 16. Cross-sectional vorticity distribution at (**a**) n = 0.85 and (**b**) n = 0.55.

4.5. Sensitivity Analysis

Sensitivity analysis was conducted to investigate the key factors influencing the friction factor. The flow rate Q, power-law index n, consistency coefficient K, fluid density ρ, and pipe diameter D were selected as independent variables. The logarithmic regression elasticity coefficient method, the parameter perturbation verification method, and the partial correlation coefficient (PCC) method were applied jointly for cross-validation to identify the dominant factors influencing frictional drag in pipes.

Based on the power function relations of friction factor to various influence parameters, a logarithmic linear regression model was established as:

$$\ln f = \ln C + a_1 \ln Q + a_2 \ln n + a_3 \ln K + a_4 \ln \rho + a_5 \ln D \tag{12}$$

where f is the friction factor, C is a constant, and a_1, a_2, a_3, a_4, and a_5 represent the elasticity coefficients corresponding to each parameter, expressed as

$$a_i = \frac{\partial \ln f}{\partial \ln x_i} = \frac{df/f}{dx_i/x_i} \tag{13}$$

where x_i denotes the i-th input parameter. In physics, this means that the friction factor f changes by a_i% on average when the parameter x_i increases by 1%.

As shown in Figure 17, the model predictions are in good agreement with the actual values, with a coefficient of determination R^2 of 0.968. This indicates that the model can accurately reveal the variation patterns of the friction factor within the investigated parameter range. The elasticity coefficients of each parameter were derived from the regression results. As shown in Figure 18, the parameter sensitivity order is $n > D > \rho > Q > K$, and the sign indicates the direction of the influence of the parameter's influence on f. These results indicate that fluid rheological properties and pipe geometry are the primary factors governing variation in the pipe friction factor.

To evaluate the robustness of the regression analysis results, four representative baseline cases were further selected, as shown in Table 4, and local perturbations of ±1%, ±3%, and ±5% were applied to each parameter. Figure 19 shows the variations in the friction factors caused by the perturbations in each parameter, yielding a sensitivity ranking of $n > D > Q > \rho \approx K$. The sensitivity rankings obtained for the four baseline cases show good consistency, confirming the reliability of the sensitivity analysis results.

Table 4. Data for the four selected base cases.

Base Case	ρ_0 (kg m^{-3})	K_0	n_0	q_0 (L min^{-1})	D_0 (m)
(a)	1009.6	0.04	0.64	320	0.042
(b)	1009.6	0.05	0.55	220	0.042
(c)	1009.6	0.05	0.64	220	0.042
(d)	1009.6	0.2	0.64	320	0.042

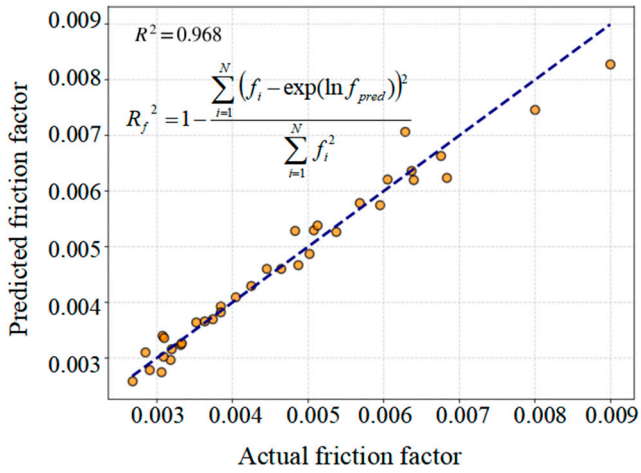


Figure 17. Comparison between predicted and actual friction factors.

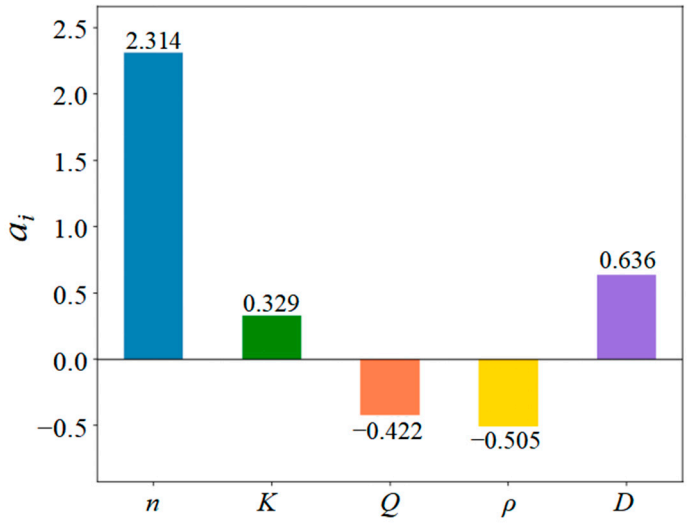


Figure 18. Sensitivity of each parameter to the friction factor, obtained by the logarithmic regression elasticity coefficient method.

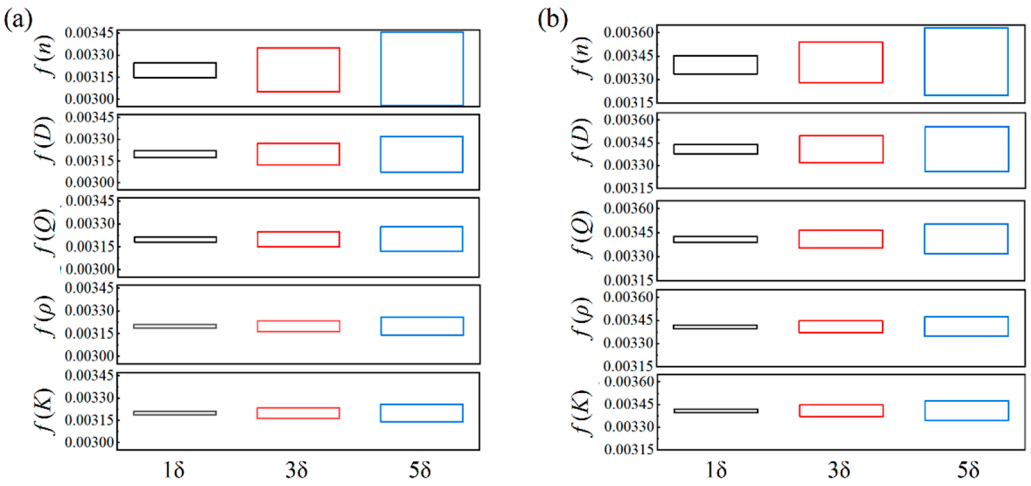


Figure 19. *Cont*.

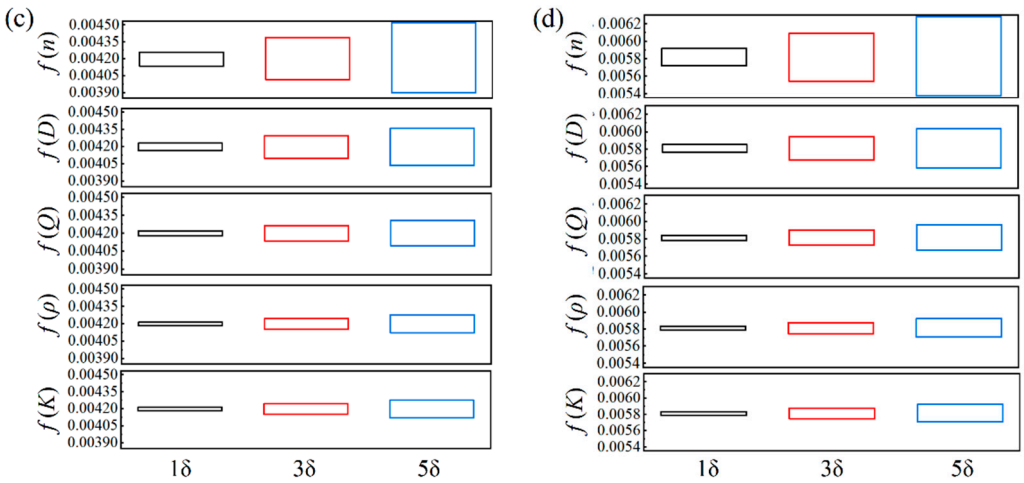


Figure 19. Variation in friction factor for four base cases ((**a**–**d**) as in Table 4) with parameters changing by 1δ (black), 3δ (red) and 5δ (blue).

Considering the possible correlations among the input parameters, the PCC method is employed to analyze the independent influence of each parameter on the friction factor while keeping other variables constant. The system is supposed to contain five input parameters, X_1, X_2, X_3, X_4, and X_5, with Y being the response variable. The partial correlation coefficients can be calculated from the inverse matrix of the covariance matrix. Letting the inverse matrix of the joint covariance matrix be $\Omega = \sum^{-1}$, the partial correlation coefficient between the i-th parameter and the response variable can be expressed as

$$PCC_{X_i,Y|X_{others}} = -\frac{\omega_{i,Y}}{\sqrt{(\omega_{i,i})(\omega_{Y,Y})}} \tag{14}$$

where $\omega_{i,\ Y}$ is the element in the i-th row and Y-th column of the inverse matrix Ω, $\omega_{i,\ i}$, $\omega_{Y,\ Y}$ are the corresponding diagonal elements, and the PCC value range is from -1 to 1, with its sign indicating the direction of the correlation. Therefore, a larger $|PCC|$ indicates a more pronounced independent influence of the parameter on the response variable.

Figure 20 shows the absolute values of the partial correlation coefficients, which indicate the influence of each parameter on the friction factor. The parameter sensitivity is ranked as $n > D > Q > K > \rho$. Therefore, discrepancies exist among the three methods in the rankings of flow rate, density, and consistency coefficient because they treat parameter correlations and local nonlinear responses differently. Based on the integrated results obtained using the three methods, the final sensitivity ranking of the pipe friction factor was determined to be $n > D > \{Q,\rho\} > K$. These results suggest that, during pipeline transport of fracturing fluids, priority should be given to controlling the fluid power-law index and selecting an appropriate pipe diameter.

The parameter sensitivity ranking obtained in this study corresponds to an overall generalized Reynolds number range of approximately 3500–53,000, and its general applicability to a broader range of flow conditions requires further validation. Abou-Kassem et al. [50] conducted a sensitivity analysis of rheological parameters for non-Newtonian pipe flow and found that the turbulent frictional pressure loss was particularly sensitive to variations in the flow behavior index n. This finding is generally consistent with the results from the present study. However, their study employed a yield-power-law fluid model and considered different parameter ranges. Future work may extend the investigated ranges of Re_g and rheological parameters and incorporate global sensitivity analysis with additional experimental data to further validate the sensitivity ranking obtained in the present study.

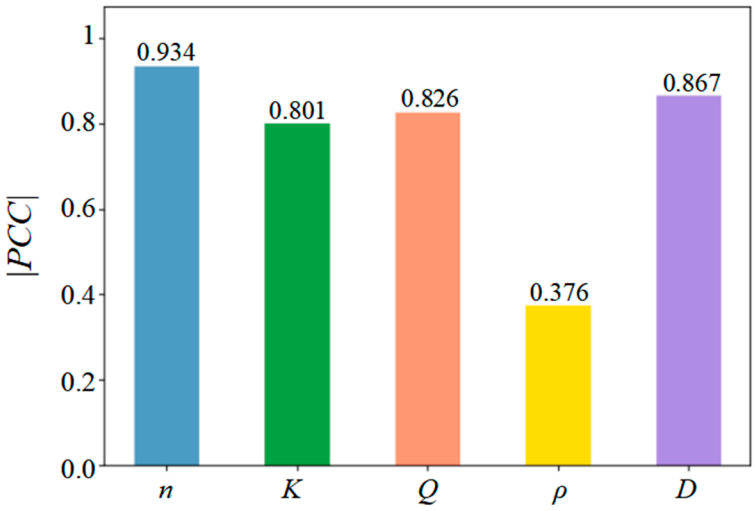


Figure 20. Sensitivity of each parameter to the friction factor, obtained by the partial correlation coefficient method.

5. Conclusions

Focusing on the turbulent frictional behaviors of weighted fracturing fluids in pipes for deep oil and gas development, this study systematically investigated the frictional behaviors of non-weighted and weighted fracturing fluids under various flow conditions using pipe flow experiments, rheological tests, and LES. The effects of rheological parameters, fluid density, pipe diameter, and flow rate on frictional drag were revealed, and parameter sensitivity analysis was carried out for cross-validation between experiments and numerical simulations. The main conclusions are as follows.

(1) For unweighted fracturing fluids, polymer molecular weight and zero-shear viscosity exhibit optimal ranges for drag reduction. Under the same zero-shear viscosity conditions, the PAM solution with a medium molecular weight of 600×10^4–700×10^4 achieves the best drag reduction effectiveness, with a maximum drag reduction rate of 62%. However, when the molecular weight is too high at 800×10^4–900×10^4, molecular chain entanglement intensifies, leading to an increase in viscous energy dissipation and a decrease in the drag reduction rate to 56%. A lower zero-shear viscosity results in a higher drag reduction rate at high flow rates. However, the differences among samples with various viscosities gradually diminish as the flow rate increases. This behavior may be associated with changes in the viscous resistance of the fluid resulting from variations in PAM concentration and zero-shear viscosity.

(2) For weighted fracturing fluids, pronounced differences in drag-reduction performance were observed among different weighting-salt systems. These differences should be regarded as the combined effects of multiple formulation factors, including weighting salt type, system density, polymer concentration, and rheological properties. Among the four weighted systems, the 20% KCl system exhibits the best drag reduction effectiveness, that is, a 64.8% drag reduction rate at 90 L/min, followed by the $CaCl_2$ systems at 57.7% and 49.4%, and the $CaBr_2$ system exhibited the lowest drag reduction rate of 42.3%. Therefore, the formulation of weighted fracturing fluids should balance the density required to provide sufficient hydrostatic pressure against the need to maintain favorable drag-reduction performance.

(3) Within the generalized Newtonian power-law LES framework and the parameter ranges investigated in this study, the power-law index n in the generalized Newtonian fluid model is the dominant parameter influencing frictional drag. Parameter sensitivity analysis shows that the sensitivity of frictional drag to each parameter is

ranked as $n > D > \{Q,\rho\} > K$. A stronger shear-thinning effect at lower n results in a larger near-wall velocity gradient and more vigorous turbulent fluctuations, thereby reducing the friction factor.

These research findings provide theoretical guidance for determining the flow parameters and physical property parameters of fracturing fluid in engineering to achieve lower pressure drops in pipe flow for deep and ultra-deep fracturing operations. It is recommended to give priority to weighting salts such as KCl that have a weaker inhibitory effect on polymer drag reduction, and to maintain polymer molecular weights within the optimal interval while ensuring that hydrostatic pressure requirements are satisfied. According to the parameter sensitivity ranking, the appropriate power-law index and pipe diameter should be determined first to meet the wellhead pressure conditions. In the future, viscoelastic constitutive models (e.g., FENE-P) should be further incorporated into the LES framework to accurately characterize polymer elastic effects, and simulation validation should be performed with higher Reynolds numbers and field-scale pipelines.

Author Contributions: Conceptualization, J.P. and Y.G.; methodology, W.Z. and Y.F.; software, J.F. and W.Z.; investigation, X.Q. and L.L.; formal analysis, L.W.; writing—original draft preparation, W.Z. and Y.F.; writing—review and editing, Y.F. and Z.L.; project administration, J.P. and L.W.; funding acquisition, J.P. and Y.G. All authors have read and agreed to the published version of the manuscript.

Funding: This research was funded by the Major Science and Technology Project of China National Petroleum Corporation, "Oil Testing and Transformation of Ultra Deep Clastic Rock Reservoirs and Key Technology Research for Oil and Gas Production", grant number 2023ZZ14YJ07.

Data Availability Statement: The datasets presented in this article are not readily available because the data are part of an ongoing study. Requests to access the datasets should be directed to the corresponding authors.

Conflicts of Interest: Authors Jianxin Peng, Jueyong Feng, Xin Qiao, and Lili Li were employed by the company Petro China Tarim Oilfield Company and company PetroChina Company Limited. Authors Ying Gao and Liwei Wang were employed by the company Research Institute of Petroleum Exploration and Development. The remaining authors declare that the research was conducted in the absence of any commercial or financial relationships that could be construed as a potential conflict of interest.

References

1. Ai, K.; Duan, L.; Gao, H.; Jia, G. Hydraulic fracturing treatment optimization for low permeability reservoirs based on unified fracture design. *Energies* **2018**, *11*, 1720. [CrossRef]
2. Wu, Z.; Cui, C.; Jia, P.; Wang, Z.; Sui, Y. Advances and challenges in hydraulic fracturing of tight reservoirs: A critical review. *Energy Geosci.* **2022**, *3*, 427–435. [CrossRef]
3. Comeaux, B.; Daulton, D. Challenging deepwater with weighted fluid. *Offshore* **2007**, *67*, 38–42.
4. Simms, L.M.; Clarkson, B.A.; Navaira, G. Weighted frac fluids for lower-surface treating pressures. In Proceedings of the SPE International Symposium and Exhibition on Formation Damage Control, Lafayette, LA, USA, 13–15 February 2008; SPE-112531-MS. [CrossRef]
5. Zhao, M.; Yang, Z.; Meng, X.; Wang, X.; Wang, Z.; Xu, Z.; Wu, Y.; Dai, C. Preparation and performance evaluation of weighted gel fracturing fluid with delayed cross-linking property for ultradeep reservoir. *Energy Fuels* **2024**, *38*, 19539–19547. [CrossRef]
6. Bai, H.; Zhou, F.; Liu, X.; Xin, X.; Zhao, H.; Ding, Z.; Wang, Y.; Wang, X.; Li, X.; Li, W.; et al. Study on pH-responsive delayed, cross-linking and weighted fracturing fluid. *Molecules* **2024**, *29*, 5847. [CrossRef]
7. Wang, X.; Song, Y.; Wu, P.; Zhang, G.; Guo, J.; Li, Y. Rheological properties of hydroxypropyl guar gum fracturing fluids: Effects of cross-linking agents. *Carbohydr. Polym.* **2025**, *366*, 123837. [CrossRef]
8. Yang, X.; Chen, A.; Mao, J.; Zhang, C.; Wang, J.; Fu, M.; Zhang, H.; Wang, J.; Song, X.; Zhang, Y.; et al. Synthetic polymer fracturing fluid weighted by sodium formate enables fracture stimulations in ultra-high pressure and high-temperature reservoir. *Fuel* **2023**, *353*, 129170. [CrossRef]

9. Toms, B.A. Some observations on the flow of linear polymer solutions through straight tubes at large Reynolds numbers. In *Proceedings of the First International Congress on Rheology*; North-Holland: Amsterdam, The Netherlands, 1949; Volume 2, pp. 135–141.
10. Virk, P.S. Drag reduction fundamentals. *AIChE J.* **1975**, *21*, 625–656. [CrossRef]
11. Lumley, J.L. Drag reduction by additives. *Annu. Rev. Fluid Mech.* **1969**, *1*, 367–384. [CrossRef]
12. Choueiri, G.H.; Lopez, J.M.; Hof, B. Exceeding the asymptotic limit of polymer drag reduction. *Phys. Rev. Lett.* **2018**, *120*, 124501. [CrossRef]
13. Escudier, M.P.; Presti, F.; Smith, S. Drag reduction in the turbulent pipe flow of polymers. *J. Non-Newton. Fluid Mech.* **1999**, *81*, 197–213. [CrossRef]
14. Donohue, G.L.; Tiederman, W.G.; Reischman, M.M. Flow visualization of the near-wall region in a drag-reducing channel flow. *J. Fluid Mech.* **1972**, *56*, 559–575. [CrossRef]
15. White, C.M.; Mungal, M.G. Mechanics and prediction of turbulent drag reduction with polymer additives. *Annu. Rev. Fluid Mech.* **2008**, *40*, 235–256. [CrossRef]
16. Motozawa, M.; Sawada, T.; Ishitsuka, S.; Iwamoto, K.; Ando, H.; Senda, T.; Kawaguchi, Y. Experimental investigation on streamwise development of turbulent structure of drag-reducing channel flow with dosed polymer solution from channel wall. *Int. J. Heat Fluid Flow* **2014**, *50*, 51–62. [CrossRef]
17. Le Brun, N.; Zadrazil, I.; Norman, L.; Bismarck, A.; Markides, C.N. On the drag reduction effect and shear stability of improved acrylamide copolymers for enhanced hydraulic fracturing. *Chem. Eng. Sci.* **2016**, *146*, 135–143. [CrossRef]
18. Habibpour, M.; Clark, P.E. Drag reduction behavior of hydrolyzed polyacrylamide/xanthan gum mixed polymer solutions. *Pet. Sci.* **2017**, *14*, 412–423. [CrossRef]
19. Wang, L.; Wang, D.; Shen, Y.; Lai, X.; Guo, X. Study on properties of hydrophobic associating polymer as drag reduction agent for fracturing fluid. *J. Polym. Res.* **2016**, *23*, 235. [CrossRef]
20. Jing, X.; Liu, Y.; Li, W.; Xu, Y.; Huang, Z. Using water-miscible nonionic hydrophobic monomer associating HPAM as drag reducing agent. *J. Appl. Polym. Sci.* **2019**, *136*, 48362. [CrossRef]
21. Jing, X.; Liu, Y.; Zhao, W.; Pu, J. Synthesis and drag reduction properties of a hydrophobically associative polymer containing ultra-long side chains. *BMC Chem.* **2023**, *17*, 48. [CrossRef]
22. Qiu, X.V.; Martch, E.; Morgenthaler, L.N.; Adams, J.; Vu, H. Design criteria and application of high-density, brine-based fracturing fluid for deepwater frac packs. In Proceedings of the SPE Annual Technical Conference and Exhibition, New Orleans, LA, USA, 4–7 October 2009; SPE-124704-MS. [CrossRef]
23. Gupta, D.V.; Carman, P.S.; Venugopal, R. High-density brine-based fracturing fluid for ultra-deep fracturing stimulation. In Proceedings of the SPE Annual Technical Conference and Exhibition, San Antonio, TX, USA, 8–10 October 2012; SPE-159822-MS. [CrossRef]
24. Yang, X.; Mao, J.; Zhang, W.; Zhang, H.; Zhang, Y.; Ouyang, D.; Chen, Q.; Lin, C.; Zhao, J. Tertiary cross-linked and weighted fracturing fluid enables fracture stimulations in ultra high pressure and temperature reservoir. *Fuel* **2020**, *268*, 117222. [CrossRef]
25. Mao, J.; Liao, Z.; Jiang, J.; Yang, X.; Zhang, Y.; Tang, Y.; Liu, P.; Zhang, H.; Xue, J.; Mao, J.; et al. One practical $CaCl_2$-weighted fracturing fluid for high-temperature and high-pressure reservoir. *Pet. Sci. Technol.* **2022**, *40*, 2877–2889. [CrossRef]
26. Liao, Z.; Chen, F.; Deng, Y.; Wang, K.; von Gunten, K.; He, Y.; Zhong, C. Organic weighting hydraulic fracturing fluid: Complex interactions between formate salts, hydroxy carboxylate acid, and guar. *SPE J.* **2022**, *27*, 2334–2351. [CrossRef]
27. Liang, T.; Yang, Z.; Zhou, F.; Liu, Z.; Qu, H.; Yang, K.; Sun, J. A new approach to predict field-scale performance of friction reducer based on laboratory measurements. *J. Pet. Sci. Eng.* **2017**, *159*, 927–933. [CrossRef]
28. Sureshkumar, R.; Beris, A.N.; Handler, R.A. Direct numerical simulation of the turbulent channel flow of a polymer solution. *Phys. Fluids* **1997**, *9*, 743–755. [CrossRef]
29. Dimitropoulos, C.D.; Dubief, Y.; Shaqfeh, E.S.G.; Moin, P.; Lele, S.K. Direct numerical simulation of polymer-induced drag reduction in turbulent boundary layer flow. *Phys. Fluids* **2005**, *17*, 011705. [CrossRef]
30. Li, C.F.; Sureshkumar, R.; Khomami, B. Influence of rheological parameters on polymer induced turbulent drag reduction. *J. Non-Newton. Fluid Mech.* **2006**, *140*, 23–40. [CrossRef]
31. Sid, S.; Dubief, Y.; Terrapon, V.E. Two-dimensional dynamics of elasto-inertial turbulence and its role in polymer drag reduction. *Phys. Rev. Fluids* **2018**, *3*, 011301. [CrossRef]
32. Martinez Ibarra, A.; Park, J.S. Transition to turbulence in viscoelastic channel flow of dilute polymer solutions. *J. Fluid Mech.* **2023**, *976*, A28. [CrossRef]
33. Poole, R.J. Inelastic and flow-type parameter models for non-Newtonian fluids. *J. Non-Newton. Fluid Mech.* **2023**, *320*, 105106. [CrossRef]
34. Owolabi, B.E.; Lin, C.A.; Poole, R.J. On the application of generalised Newtonian fluids in the modelling of drag-reducing rigid polymers. *J. Non-Newton. Fluid Mech.* **2023**, *319*, 105089. [CrossRef]
35. Malin, M.R. Turbulent pipe flow of power-law fluids. *Int. Commun. Heat Mass Transf.* **1997**, *24*, 977–988. [CrossRef]

36. Pinho, F.T. A GNF framework for turbulent flow models of drag reducing fluids and proposal for a k–ε type closure. *J. Non-Newton. Fluid Mech.* **2003**, *114*, 149–184. [CrossRef]
37. Cruz, D.O.A.; Pinho, F.T. Turbulent pipe flow predictions with a low Reynolds number k–ε model for drag reducing fluids. *J. Non-Newton. Fluid Mech.* **2003**, *114*, 109–148. [CrossRef]
38. Masoudian, M.; Kim, K.; Pinho, F.T.; Sureshkumar, R. A viscoelastic k–ε–v^2–f turbulent flow model valid up to the maximum drag reduction limit. *J. Non-Newton. Fluid Mech.* **2013**, *202*, 99–111. [CrossRef]
39. McDermott, M.; Resende, P.R.; Wilson, M.C.T.; Afonso, A.M.; Harbottle, D.; de Boer, G. An improved k–ω turbulence model for FENE-P fluids without friction velocity dependence. *Int. J. Heat Fluid Flow* **2021**, *90*, 108799. [CrossRef]
40. Niazi, M.; Ashrafizadeh, S.N.; Hashemabadi, S.H. Improving the prediction of turbulent kinetic energy for drag reduction in turbulent viscoelastic pipe flow. *Phys. Fluids* **2024**, *36*, 063101. [CrossRef]
41. Gnambode, P.S.; Orlandi, P.; Ould-Rouiss, M.; Nicolas, X. Large-eddy simulation of turbulent pipe flow of power-law fluids. *Int. J. Heat Fluid Flow* **2015**, *54*, 196–210. [CrossRef]
42. Amani, E.; Ahmadpour, A.; Aghajari, M. Large-eddy simulation of turbulent non-Newtonian flows: A comparison with state-of-the-art RANS closures. *Int. J. Heat Fluid Flow* **2023**, *99*, 109076. [CrossRef]
43. Taghvaei, M.; Amani, E. Wall-modeled large-eddy simulation of turbulent non-Newtonian power-law fluid flows. *J. Non-Newton. Fluid Mech.* **2023**, *322*, 105136. [CrossRef]
44. Yang, Z.; Wang, H.; Huang, Z.; Jiao, W.; Zhao, B.; Liu, X.; Na, X. Hydrodynamic characteristics of a cylinder with angular velocity during low-speed water entry. *Ocean Eng.* **2026**, *355*, 125126. [CrossRef]
45. Dai, S.; Tang, D.; Younis, B.A.; Xiong, C. Large-eddy simulations of oscillatory flow around a cylinder at high Keulegan–Carpenter and Reynolds numbers. *Acta Mech. Sin.* **2026**, *42*, 325204. [CrossRef]
46. Nicoud, F.; Ducros, F. Subgrid-scale stress modelling based on the square of the velocity gradient tensor. *Flow Turbul. Combust.* **1999**, *62*, 183–200. [CrossRef]
47. Sorgun, M.; Muftuoglu, T.D.; Gucuyener, I.H. Friction factor estimation for turbulent flow of Herschel–Bulkley and power law fluids in pipes. *J. Pet. Sci. Eng.* **2022**, *211*, 110044. [CrossRef]
48. El Khoury, G.K.; Schlatter, P.; Noorani, A.; Fischer, P.F.; Brethouwer, G.; Johansson, A.V. Direct numerical simulation of turbulent pipe flow at moderately high Reynolds numbers. *Flow Turbul. Combust.* **2013**, *91*, 475–495. [CrossRef]
49. Singh, J.; Rudman, M.; Blackburn, H.M. Reynolds number effects in pipe flow turbulence of generalized Newtonian fluids. *Phys. Rev. Fluids* **2018**, *3*, 094607. [CrossRef]
50. Abou-Kassem, A.J.; Bizhani, M.; Kuru, E. A review of methods used for rheological characterization of yield-power-law (YPL) fluids and their impact on the assessment of frictional pressure loss in pipe flow. *Geoenergy Sci. Eng.* **2023**, *229*, 212050. [CrossRef]

Disclaimer/Publisher's Note: The statements, opinions and data contained in all publications are solely those of the individual author(s) and contributor(s) and not of MDPI and/or the editor(s). MDPI and/or the editor(s) disclaim responsibility for any injury to people or property resulting from any ideas, methods, instructions or products referred to in the content.